Planar thermal Hall effect of topological bosons in the Kitaev magnet α-RuCl3

Peter Czajka
Princeton University https://orcid.org/0000-0001-9938-0952
Tong Gao
Princeton University https://orcid.org/0000-0002-8157-3892
Max Hirschberger
The University of Tokyo
Paula Lampen-Kelley
Univ. Tennessee
Arnab Banerjee
Purdue University https://orcid.org/0000-0002-3088-6071
Nicholas Quirk
Princeton University https://orcid.org/0000-0001-9612-5817
David Mandrus
Oak Ridge National Laboratory
Stephen Nagler
Oak Ridge National Laboratory https://orcid.org/0000-0002-7234-2339
N. Phuan Ong (npo@princeton.edu)
Princeton University https://orcid.org/0000-0001-7166-1058

Research Article

Keywords:

Posted Date: April 27th, 2022

DOI: https://doi.org/10.21203/rs.3.rs-1546389/v1

Additional Declarations: There is **NO** Competing Interest.

Version of Record: A version of this preprint was published at Nature Materials on November 17th, 2022. See the published version at https://doi.org/10.1038/s41563-022-01397-w.

Planar thermal Hall effect of topological bosons in the Kitaev magnet α-$RuCl_3$

Peter Czajka[1], Tong Gao[1], Max Hirschberger[2], Paula Lampen-Kelley[3,4], Arnab Banerjee[6], Nicholas Quirk[1], David G. Mandrus[3,4], Stephen E. Nagler[5], and N. P. Ong[1,*]

[1]*Dept. of Physics, Princeton University, Princeton, NJ 08544, USA*

[2]*Dept. of Applied Physics, The University of Tokyo, Tokyo 113-8656, Japan*

[3]*Dept. Mater. Science and Engineering, Univ. of Tennessee, Knoxville, Tennessee 37996, USA*

[4]*Mater. Sci. and Technol. Division, Oak Ridge National Lab., Oak Ridge, Tennessee 37831, USA*

[5]*Neutron Scattering Division, Oak Ridge National Lab., Oak Ridge, Tennessee 37831, USA*

[6]*Dept. Physics and Astronomy, Purdue University, West Lafayette, IN 47907-2036*

[*]*Corresponding author. Email: npo@princeton.edu*

(Dated: April 7, 2022)

In the field of quantum spin liquids [1–3], the honeycomb magnet α-$RuCl_3$ has attracted considerable interest because it is proximate to the Kitaev Hamiltonian $\mathcal{H}_K$ [4–12]. In 2006, Kitaev [13] published the exact solution for the ground state of $\mathcal{H}_K$, and found that the excitations are Majoranas and vortices. The thermal Hall conductivity κ_{xy} of Majorana fermions is predicted to be half-quantized [13]. This effect has been reported in α-$RuCl_3$ [17, 18], but this observation has proven difficult to reproduce [19, 20] and remains highly controversial. We report detailed measurements of the Onsager-like planar thermal Hall conductivity κ_{xy} in α-$RuCl_3$, a spin-liquid candidate of topical interest. With the thermal current $\mathbf{J}_\mathrm{Q}$ and magnetic field $\mathbf{B} \parallel$ a (zigzag axis), the observed κ_{xy}/T varies strongly with temperature T (1-10 K). Using a novel fitting procedure, we show that this temperature dependence matches the distinct form expected for topological bosonic modes in a Chern insulator-like model. Our analysis yields band energies that are in agreement with earlier experiments and that the excitations evolve into increasingly magnon-like modes at high B with a Chern number ~ 1. The bosonic character is incompatible with half-quantization of κ_{xy}/T.

The thermal Hall effect provides a powerful probe of spin excitations, for e.g. in the pyrochlores $Lu_2V_2O_7$ [14] and $Tb_2Ti_2O_7$ [15] and the kagome magnet Cu(1-3, bdc) [16]. In 2018, evidence for a half-quantized κ_{xy} in α-$RuCl_3$ in the narrow interval $3.7 < T < 5$ K was reported in Ref. [17]. Half-quantization of κ_{xy}/T was also observed [18] with $\mathbf{B} \parallel \mathbf{a}$ but in a narrow field interval distinct from that in Ref. [17]. Subsequently, the authors of Ref. [19] reported that the planar κ_{xy} was strongly T dependent showing no trace of half-quantized behavior. In this report, large oscillations of κ_{xx} were observed with maximal amplitude within the window $7 < H < 11.5$ T. A third group recently reported a κ_{xy} signal consistent with half-quantization in the planar geometry [20], but the large uncertainties in their data call into question their claim of robustness. The conflicting results reflect the weak signal and large hysteretic and magnetocaloric effects below 4 K.

Adopting measures (Supplemental Information) [21] to mitigate these distortions, we have obtained κ_{xy} over a broad interval of T (0.5 to 10 K). Our results point to a view of κ_{xy} categorically distinct from the half-quantized picture. We show that κ_{xy} originates from bosonic edge-mode excitations that become topological magnons at large B. Whereas

fermionic edge modes have been investigated intensively in quantum Hall systems, our experiment is the first quantitative demonstration of neutral bosonic edge modes in a magnetic insulator.

In the experiment, both the thermal current $\mathbf{J}_{\rm Q}$ and $\mathbf{B}$ are applied $\parallel \hat{\mathbf{x}} \parallel \mathbf{a}$. During each run lasting 8-10 h, B is incremented in steps $\delta B_{\rm step} = 0.2$ T from -13 to +13 T (and back to -13 T) while T is regulated within ± 1 mK of its set-point. We adopt a step-probe protocol [21] in which measurements of the sensors $T_{\rm A}$, $T_{\rm B}$ and $T_{\rm C}$ are delayed by 150 s after each step-change. The protocol rigorously excludes contamination by the large transients caused by magnetocaloric and eddy-current heating effects. Hysteretic artefacts are eliminated by combining field sweep-up and -down curves. The 3 readings determine the values of λ_{yx} and λ_{xx} at each B.

Figure 1 (a) shows the explicitly B-antisymmetric thermal Hall signal $\Delta T_{\rm H}^{\rm asym}$ (proportional to the thermal Hall resistivity λ_{yx}) measured at 7.5 K in an in-plane $\mathbf{B} \parallel \hat{\mathbf{x}}$ (inset). At each B, the thermal Hall signal is obtained by combining the two readings $T_{\rm B} - T_{\rm C}$ and $T_{\rm A} - T_{\rm C}$, and field-antisymmetrizing [21]. In Panel (b), the color map provides an overview of how λ_{yx} varies over the B-T plane. The large-λ_{yx} region above 4 K (red area) tapers to a thin neck at 7.5 T as T decreaes to 1 K. Below 2.5 K, λ_{yx} becomes slightly negative in the small region shown in blue. The evolution of the field profiles of λ_{yx} is shown in Fig. 1c. At 9.22 K, the profile features a broad peak that narrows dramatically as $T \rightarrow 3.65$ K. At high B (> 10 T), λ_{yx} is strongly suppressed to values below our resolution for $T < 4$ K.

From the matrix inversion $\kappa_{ij} = [\lambda^{-1}]_{ij}$, we derive the curves of κ_{xy}/T vs. B which display a peak in the field profile (Fig. 1d). In the regime $B > 10$ T and $T < 4$ K, the matrix inversion leads to large uncertainties (caused by multiplying a near-zero λ_{yx} by a factor of $\sim 10^3$ [21]). Over the interval $0.5 < T < 10$ K, κ_{xy}/T does not show evidence of half-quantization (dashed line). Instead, the dominant feature is the strong T dependence of κ_{xy}/T.

Figure 2 shows how κ_{xy}/T varies with T with B fixed at between 5 and 10 T. At each value of B, κ_{xy}/T falls monotonically towards zero as T decreases below 10 K. We have found that the steep T dependence is in quantitative agreement with edge modes populated by bosons (solid curves).

First, a planar thermal Hall effect that is odd in $\mathbf{B}$ is quite unexpected. In topological materials, however, the emergence of a Berry curvature $\mathbf{\Omega}$ that reverses sign with $\mathbf{B}$ can

lead to a planar (electrical) Hall response, as seen in $ZrTe_5$ [22]. For this purpose, we would need $\mathbf{\Omega} \parallel \hat{\mathbf{c}}^*$ (normal to the honeycomb layer) as well as to reverse sign with $\mathbf{B} \parallel \mathbf{a}$.

Recent calculations have shown that $\mathbf{\Omega}$ indeed emerges in α-$RuCl_3$ with high-intensity spots near each of the K points in the Brillouin zone (BZ) [23–25] (Fig. 3a, inset). At large B, the excitations, called topological magnons, occupy bands in which the Chern number $\mathcal{C}_n$ alternates in sign [23–25]. Crucially, when $\mathbf{B} \parallel \mathbf{a}$, $\mathbf{\Omega}$ reverses sign with $\mathbf{B}$ [25, 30, 31].

In a 2D magnet with finite $\mathbf{\Omega}$, the thermal Hall conductivity is given by [26, 27]

$$\frac{\kappa_{xy}}{T} = \frac{1}{\hbar V} \sum_{n,\mathbf{k}} \Omega_{n,z}(\mathbf{k}) \int_{\varepsilon_{n,\mathbf{k}}}^{\infty} d\varepsilon \frac{(\varepsilon - \mu)^2}{T^2} \left(-\frac{d\rho}{d\varepsilon} \right), \tag{1}$$

where the sum is over bands with dispersion $\varepsilon_{\mathbf{k}}$ and Berry curvature $\mathbf{\Omega}_n$, ρ is the distribution function of the relevant excitaion, V is the sample volume, μ the chemical potential and $\hbar = h/2\pi$ with h the Planck constant.

Semiclassically, we may regard a wave-packet subject to $\mathbf{\Omega}$ and the force $-\nabla U$ exerted by the wall potential U [27] (Fig. 3a, inset). The anomalous velocity $\mathbf{v}_A = -\nabla U \times \mathbf{\Omega}$ drives a circulating thermal current around the edges. A thermal gradient $-\nabla T \parallel \hat{\mathbf{x}}$ unbalances the excitation density between the warm and cool edges ($\parallel \hat{\mathbf{y}}$), which leads to a net thermal current $\mathbf{J}_{\mathrm{Q}} \parallel \hat{\mathbf{y}}$ (Fig. 3c). Crucially, the reversal of $\mathbf{\Omega}$ induced by reversing $\mathbf{B}$ leads to an Onsager planar thermal Hall current.

If the excitations are fermions, Eq. 1 yields the (T-independent) Kane-Fisher result [28, 29]

$$\frac{\kappa_{xy}}{T} = \frac{\pi^2}{3} \frac{k_B^2}{h} \nu, \quad (\nu \in \mathbb{Z}). \tag{2}$$

where k_B is Boltzmann's constant.

By contrast, for bosons, Eq. 1 yields a very strong T dependence. In units of the universal thermal conductance k_B^2/h (and setting $\mu = 0$), Eq. 1 simplifies to

$$\frac{\mathcal{K}_{\mathrm{H}}}{T} \equiv \frac{\kappa_{xy}/T}{k_B^2/h} = \sum_n \mathcal{C}_n \, c_2^{(n)}(\omega_n, T) \tag{3}$$

The function $c_2^{(n)}(\omega_n, T)$ is defined as [26, 27]

$$c_2^{(n)}(\omega_n, T) = \int_{u_{0n}}^{\infty} du \, u^2 (-d\rho/du), \quad (u_{0n} = \beta\omega_n(\mathbf{k})), \tag{4}$$

where $\rho = 1/(\mathrm{e}^u - 1)$ and $\beta = 1/(k_B T)$. The lowest band is nearly flat [25]. Adopting the flat-band approximation, we used the winding-number equation $2\pi\mathcal{C}_n = \int_{\mathrm{BZ}} d^2k \; \Omega_{n,z}(\mathbf{k})$ to relate $\Omega_{n,z}$ to $\mathcal{C}_n$.

At low T, we retain the 2 lowest bands in Eq. 3 (Fig. 3a and Ref. [21]). Assuming that their Chern numbers alternate in sign ($\mathcal{C}_1 = -\mathcal{C}_2$), we have

$$\frac{\mathcal{K}_{\rm H}}{T} = \mathcal{C}_1 \left[c_2^{(1)}(\omega_1, T) - c_2^{(2)}(\omega_2, T) \right]. \tag{5}$$

The overall scale of $\mathcal{K}_{\rm H}/T$ is fixed by $\mathcal{C}_1$.

We find that Eq. 5 provides close fits to the observed κ_{xy}/T over a broad range of B (the fits were carried out on $\kappa_{xy}^{\rm 2D} = \kappa_{xy} d$ with $d = 5.72$ Å). In Fig. 2, the fits are shown as the solid curves. We have found that slight deviations from the fits (grey circles) reveal important information on the excitations.

For $B < 6.8$ T, κ_{xy}/T displays a weak, negative deviation (dip) below 3 K (in the blue region in Fig. 1b). The expanded view in Fig. 3b shows the dips in 4 traces of κ_{xy}/T vs. T. The negative dips imply that, once we enter the ordered phase (below 7 T), the spin excitation branches deviate from Eq. 3. The weak negative dip feature also appears in calculations of κ_{xy} (see Figs. 3 and 6 in Ref. [30]). Weak, positive deviations are also observed below ∼11 T. These deviations may represent the growth of excitations in the QSL state as $T \to 0$. Within the uncertainties, they scale with the amplitude of the oscillations in κ_{xx} [21].

Away from these deviations, the fits shown in Fig. 2 describe quite accurately the strong T dependence of κ_{xy}/T over a broad range of B. At each B, the fit yields the 2 energies ω_1 and ω_2 (in Eq. 4) as well as the dimensionless quantity $\mathcal{C}_{\rm obs}$ discussed next.

Dividing Eq. 5 across by the T-dependent factor $[c_2^{(1)}(\omega_1, T) - c_2^{(2)}(\omega_2, T)]$, we define

$$\mathcal{C}_{\rm obs} \equiv (\mathcal{K}_{\rm H}/T)/[c_2^{(1)}(\omega_1, T) - c_2^{(2)}(\omega_2, T)], \tag{6}$$

which can be compared with $\mathcal{C}_1$. $\mathcal{C}_{\rm obs}$ is plotted vs. B in Fig. 3c.

We find that $\mathcal{C}_{\rm obs}$ starts off small (~ 0.3 at 5 T) but increases to attain a plateau above 9 T. Within the experimental uncertainty, the nearest integer at the plateau is $\mathcal{C}_{\rm obs} \simeq 1$. The strong T dependence of κ_{xy}/T largely arises from the bosonic distribution in the integrand of $c_2^{(n)}$ (Eq. 4). Remarkably, once this is factored out, the overall amplitude in the polarized state at high fields is fixed by the integer $\mathcal{C}_{\rm obs} \simeq 1$.

We show next that the energy ω_1 derived from the fits of κ_{xy}/T to Eq. 1 closely agrees with the energy of the dominant sharp mode seen in electron spin resonance (ESR) [32, 33], microwave absorption [8, 34] and neutron-scattering experiments [36]. The energy of the

second band is found to be $\omega_2 \sim 50 \pm 10$ K with a large uncertainty [21]. In the field interval above B_c (from 7.3 to 14 T), α-$RuCl_3$ displays a rich magnetic resonance spectrum with 4 sharp modes (C, D, E and F) [32] superposed on a broad continuum suggestive of excitations [8, 34]. The broad continuum was observed also in microwave absorption and inelastic neutron scattering experiments [36]. At B= 7.3, the two lowest modes C and F are degenerate at 0.27 THz (1.1 meV). As B is raised to 16 T, both increase steeply to 1.1 THz (for C) and 0.9 THz (F). These modes are also seen in exact diagonalization of a 24-spin model [35]. Close to B_c, ω_1 inferred from κ_{xy}/T agrees remarkably well with the degenerate values of C and F. At large B, ω_1 is lower than C (C arises from vertical $\Delta\mathbf{q} = 0$ transitions [33] at the zone center Γ). This suggests that, as C rises steeply with B, κ_{xy} is weighted towards lower-lying excitations from elsewhere in the BZ. The curve of $\omega_1(B)$ agrees with the energy scale inferred in Ref. [11] from $\kappa_{xx}(T)$.

As discussed in Refs. [32, 33, 35], the sharp ESR mode C is increasingly dominant at large B but the broad background excitation continuum persists. From this viewpoint, the observed saturation of $\mathcal{C}_{\rm obs}$ to 1 above 9 T in Fig. 3d is physically appealing. As the dominant excitations become increasingly magnon-like, the topological Hall current, expressed as $\mathcal{C}_{\rm obs}$, approaches 1. For $B < 7$ T (zig-zag state) the vanishing of κ_{xy} (aside from the negative dip near 6.3 T) suggests that Ω is very small. Our results also conclusively rule out a phonon mechansim for the planar κ_{xy} [21].

The physical picture that emerges is that the planar κ_{xy} derives from spin excitations that live at the relatively high energy scale $\omega_1 \sim 1$ meV (11.6 K) and form a bosonic Chern insulator- like state at high B (though with μ fixed at 0 instead of inside the gap between bands). A large Berry curvature drives these excitations as an edge-mode thermal current, which results in an Onsager-type thermal Hall current whose magnitude corresponds to a Chern number of 1 at fields above 9 T and leads to a distinct T dependence for κ_{xy}/T. At all B, the bosonic character leads to strong suppression of κ_{xy} to near zero below 3 K. The strong T dependence of κ_{xy}/T precludes a fermionic description and raises serious questions about the validity of the reports of quantization. A detailed discussion of why claims of robustness are problematic is given in Ref. [21]. Finally, we note that ω_1 is not a bulk "spin gap". The sharp modes coexist with a broad continuum corresponding to spin excitations that extend well below ω_1. We emphasize that the magnons are only well-defined above $\sim$10 T [36]. As we lower B into the spin-liquid state, the excitations are increasingly less

magnon-like, as seen in the deviations from the fit to Eq. 3 as well as the steep decrease of $C_{\rm obs}$ (Fig. 3c). The deviations provide clues to the excitations in the spin-liquid state. In the low-T limit, the edge-mode engendered κ_{xy} vanishes altogether while novel bulk features emerge to define the oscillations observed in κ_{xx} [19, 37].

References

[1] Savary, L. & Balents, L., Quantum spin liquids: a review, *Rep. Prog. Phys.* **80**, 106502 (2017). doi:10.1088/0034-4885/80/1/016502

[2] Zhou, Y., Kanoda, K. & Ng, T.K. Quantum spin liquid states, *Rev. Mod. Phys.* **89**, 025003 (2017). DOI: 10.1103/RevModPhys.89.025003

[3] Hidenori Takagi, Tomohiro Takayama, George Jackeli, Giniyat Khaliullin and Stephen E. Nagler, Concept and realization of Kitaev quantum spin liquids, *Nat. Rev. Phys.* **1**, 264-280 (2019). doi.org/10.1038/s42254-019-0038-2

[4] Jackeli, G. & Khaliullin, G., Mott Insulators in the Strong Spin-Orbit Coupling Limit: From Heisenberg to a Quantum Compass and Kitaev Models, Phys. Rev. Lett. **102**, 017205 (2009).

[5] Plumb, K. W. *et al.*, α-$RuCl_3$: a spin-orbit assisted Mott Insulator on a honeycomb lattice. *Phys. Rev. B* **90**, 041112 (2014).

[6] Banerjee, A. *et al.*, Proximate Kitaev quantum spin liquid behavior in a honeycomb magnet. *Nat. Mater.* **15**, 733-740 (2016).

[7] Sears, J. A. *et al.*, Phase diagram of α-$RuCl_3$ in an in-plane magnetic field. *Phys. Rev. B* **95**, 180411 (2017).

[8] Z. Wang, S. Reschke, D. Huvonen, S.H. Do, K. Y. Choi, M. Gensch, U. Nagel, T. Room, and A. Loidl, Magnetic excitations and continuum of a possibly field-induced quantum spin liquid in α-$RuCl_3$, Phys. Rev. Lett.**119**, 227202 (2017). DOI: 10.1103/PhysRevLett.119.227202

[9] Leahy. I. A. *et al.*, Anomalous thermal conductivity and magnetic torque response in the honeycomb magnet α-$RuCl_3$, *Phys. Rev. Lett.* **118**, 187203 (2017).

[10] Banerjee, A. *et al.*, Excitations in the field-induced quantum spin liquid state of α-$RuCl_3$. npj

Quantum Materials (2018) 3:8 ; doi:10.1038/s41535-018-0079-2

[11] Hentrich, R. *et al.*, Unusual phonon heat transport in α-$RuCl_3$: Strong spin-phonon scattering and field-induced spin gap. *Phys. Rev. Lett.* **120**, 117204 (2018).

[12] Lampen-Kelley , P. *et al.*, Anisotropic susceptibilities in the honeycomb Kitaev system α-$RuCl_3$. *Phys. Rev. B* **98**, 100403 (2018).

[13] Kitaev, A., Anyons in an exactly solved model and beyond, *Ann. Phys.* **321**, 2-111 (2006).

[14] Y. Onose, T. Ideue, H. Katsura, Y. Shiomi, N. Nagaosa, Y. Tokura, Observation of the Magnon Hall Effect, *Science* **329**, 297 (2011). 10.1126/science.1188260

[15] Max Hirschberger, Jason W. Krizan, R. J. Cava, N. P. Ong, Large thermal Hall conductivity of neutral spin excitations in a frustrated quantum magnet, *Science* **348**, 106 (2015). 10.1126/science.1257340

[16] Max Hirschberger, Robin Chisnell, Young S. Lee, and N. P. Ong, Thermal Hall Effect of Spin Excitations in a Kagome Magnet, Phys. Rev. Lett.**115**, 106603 (2015). DOI: 10.1103/PhysRevLett.115.106603

[17] Kasahara, Y. *et al.*, Majorana quantization and half-integer thermal quantum hall effect in a Kitaev spin liquid. *Nature* **559**, 227-231 (2018).

[18] T. Yokoi, S. Ma, Y. Kasahara, S. Kasahara, T. Shibauchi, N. Kurita, H. Tanaka, J. Nasu, Y. Motome, C. Hickey, S. Trebst and Y. Matsuda, Half-integer quantized anomalous thermal Hall effect in the Kitaev candidate α-$RuCl_3$, *Science* **373**, 568-572 (2021). DOI: 10.1126/science.aay5551

[19] PeterCzajka, Tong Gao, Max Hirschberger, Paula Lampen-Kelley, Arnab Banerjee, Jiaqiang Yan, David G. Mandrus, Stephen E. Nagler, and N. P. Ong, Oscillations of the thermal conductivity in the spin-liquid state of α-$RuCl_3$, Nature Physics **17**, 915-919 (2021). doi.org/10.1038/s41567-021-01243-x

[20] J. A. N. Bruin, R. R. Claus, Y. Matsumoto, N. Kurita, H. Tanaka and H. Takagi, Robustness of the thermal Hall effect close to half-quantization in a field-induced spin liquid state, cond-mat arXiv:2104.12184.

[21] Supplemental Information.

[22] Liang, T. *et al..*, Anomalous Hall effect in $ZrTe_5$, *Nat. Phys.* **14**, 451-455 (2018). doi.org/10.1038/s41567-018-0078-z

[23] McClarty, P. A. and Dong, X.-Y. and Gohlke, M. and Rau, J. G. and Pollmann, F. and

Moessner, R. and Penc, K., Topological magnons in Kitaev magnets at high fields, Phys. Rev. B **98**, 060404 (2018). 10.1103/PhysRevB.98.060404

[24] Joshi, Darshan G., Topological excitations in the ferromagnetic Kitaev-Heisenberg model, Phys. Rev. B **98**, 060405 (2018). 10.1103/PhysRevB.98.060405

[25] Li Ern Chern, Emily Z. Zhang and Yong Baek Kim, Sign Structure of Thermal Hall Conductivity and Topological Magnons for In-Plane Field Polarized Kitaev Magnets, Phys. Rev. Lett.**126**, 147201 (2021). 10.1103/PhysRevLett.126.147201

[26] Ryo Matsumoto and Shuichi Murakami, Theoretical Prediction of a Rotating Magnon-Wave Packet in Ferromagnets, Phys. Rev. Lett. **106**, 197202 (2011) DOI: 10.1103/PhysRevLett.106.197202

[27] Ryo Matsumoto and Shuichi Murakami, Rotational motion of magnons and the thermal Hall effect, Phys. Rev. B**84**, 184406 (2011). DOI: 10.1103/PhysRevB.84.184406

[28] C. L. Kane and Matthew P.A. Fisher, Quantized thermal transport in the fractional quantum Hall effect, Phys. Rev. B**55**, 15 832 (1997).

[29] Yanting Teng, Yunchao Zhang, Rhine Samajdar, Mathias S. Scheurer, and Subir Sachdev, Unquantized thermal Hall effect in quantum spin liquids with spinon Fermi surfaces, Phys. Rev. Res. **2**, 033283 (2020). DOI: 10.1103/PhysRevResearch.2.033283

[30] Zhang, Emily Z. and Chern, Li Ern and Kim, Yong Baek, Topological magnons for thermal Hall transport in frustrated magnets with bond-dependent interactions, Phys. Rev. B **103**, 174402 (2021). 10.1103/PhysRevB.103.174402

[31] Franz G. Utermohlen and Nandini Trivedi, Symmetry analysis of tensors in the honeycomb lattice of edge-sharing octahedra, *Phys. Rev. B* **103**, 155124 (2021). DOI: 10.1103/PhysRevB.103.155124

[32] A. N. Ponomaryov, E. Schulze, J. Wosnitza, P. Lampen-Kelley, A. Banerjee, J.-Q. Yan, C. A. Bridges, D. G. Mandrus, S. E. Nagler, A. K. Kolezhuk, and S. A. Zvyagin, Unconventional spin dynamics in the honeycomb-lattice material α-$RuCl_3$: High-field electron spin resonance studies, Phys. Rev. B**96**, 241107(R) (2017). DOI: 10.1103/PhysRevB.96.241107

[33] A. N. Ponomaryov, L. Zviagina, J. Wosnitza, P. Lampen-Kelley, A. Banerjee, J.-Q. Yan, C. A. Bridges, D. G. Mandrus, S. E. Nagler, and S. A. Zvyagin, Nature of Magnetic Excitations in the High-Field Phase of α-$RuCl_3$. Phys. Rev. Lett.**125**, 037202 (2020). DOI: 10.1103/PhysRevLett.125.037202

[34] C. Wellm, J. Zeisner, A. Alfonsov, A. U. B. Wolter, M. Roslova, A. Isaeva, T. Doert, M. Vojta, B. Buchner and V. Kataev, Signatures of low-energy fractionalized excitations in α-$RuCl_3$ from field-dependent microwave absorption, Phys. Rev. B**98**, 184408 (2018). DOI: 10.1103/PhysRevB.98.184408

[35] Stephen M. Winter, Kira Riedl, David Kaib, Radu Coldea, and Roser Valenti, Probing α-$RuCl_3$ Beyond Magnetic Order: Effects of Temperature and Magnetic Field, Phys. Rev. Lett.**120**, 077203 (2018). DOI: 10.1103/PhysRevLett.120.077203

[36] Balz, C. *et al.*, Finite field regime for a quantum spin liquid in α-$RuCl_3$. *Phys. Rev. B* **100**, 060405(R) (2019).

[37] Inti Sodemann Villadiego, Pseudoscalar U(1) spin liquids in α-$RuCl_3$, *Phys. Rev.* B **104**, 195149 (2021). DOI: 10.1103/PhysRevB.104.195149

Methods:

The mounting procedure used for the sample follows the procedure described in detail in Ref. [19]. A photo of the crystal and thermometer setup used in this report is shown in Extended Data Fig. 1. The thermometers (RX102A) are connected to the crystal using Stycast epoxy via 5 mil Au wires (which themselves are attached to the thermometers using Ag epoxy). The ceramic heater (R = 1 kΩ) is attached directly to the crystal using Ag paint. The crystal is also attached to a brass plate using Ag paint. To avoid damage caused by the large magnetic torque above 3 Tesla, the other end of the crystal is mechanically supported using a piece of delrin (a low thermal conductivity polymer) attached using Stycast epoxy. Once mounted, the brass plate is placed onto a Janis ^{3}He insert. Special care must be taken to not over-strain the crystal at any point as even small amounts of mechanical stress may induce unwanted stacking faults in the crystal. To minimize electrical noise, all thermometers (sample and stage) are measured using Lakeshore LS372 temperature controllers. The LS372 uses an AC lock-in based method that is optimized for temperature measurements that offers significantly better resolution than DC-based Lakeshore models like the LS340 as well as conventional lock-in amplifiers.

The thermal transport tensor is calculated using a standard steady-state technique. A thermal current of known density $\mathbf{J}^q$ is applied using the 1 kΩ heater. We define $\hat{\mathbf{x}} \parallel \mathbf{J}^Q$ and $\hat{\mathbf{z}} \parallel c^*$ so $\hat{\mathbf{y}}$ is the transverse/Hall direction. The thermal resistivity matrix is analogous to the electrical equivalent and relates the applied current $\mathbf{J}^Q$ to the resulting temperature gradient ∇T:

$$-\partial_i T = \lambda_{ij} J_j^Q$$

In the experiment we measure the longitudinal and transverse temperature differences ($\Delta_x T$ and $\Delta_y T$). From these values, $\mathbf{J}^Q$, and the appropriate sample dimensions we are able to calculate all components of λ_{ij} and then invert the resulting matrix to obtain the thermal conductivity matrix $\kappa_{ij} = (\lambda^{-1})_{ij}$. We stress that it is only the field-antisymmetric component of Δ_y that is used in the above calculation and it is this value (now referred to as ΔT^{asym}) that is the most essential quantity that is measured in these experiments. Crucial steps were taken to remove all extrinsic contributions to the measured ΔT^{asym}. Our approach is to step-increase the magnetic field by 0.2 T (steps spaced by 180 s). Once a new field value is reached, we wait for the thermometers to relax to their equilibrium temperatures. Extended Data Fig. 2 shows an example of this during data collection. The transient

temperature shifts that ultimately relax are caused by eddy currents in the measurement apparatus and the unusually large magnetocaloric effects in $RuCl_3$. When analyzing the data, we choose an averaging window (light blue strip) that contains only data acquired after equilibrium is attained. More information about the technical details of our measurements can be found in the supplementary material [21].

Acknowledgments:

We acknowledge useful discussions with Inti Sodemann and Senthil Todadri. P.C., T.G., N.Q., and N.P.O., and the thermal transport experiments were supported by the US Department of Energy (DE-SC0017863), a MRSEC award from the US National Science Foundation (DMR 2011750), and by the Gordon and Betty Moore Foundation EPiQS initiative through grant GBMF4539. A.B. and S.E.N. were supported by the DOE, Office of Science, Scientific User Facilities Division. P.L.-K. and D.G.M. were supported by the Gordon and Betty Moore Foundation's EPiQS initiative through grant GBMF9069.

Author contributions:

P.C. performed the measurements and analyzed the data with N.P.O. P.C., T.G., and N.P.O. conceptualized the experiment, which employs a methodology developed by them and M.H. The crystal was grown and characterized at Oak Ridge National Laboratory by P.L.-K., A.B., D.G.M., and S.E.N. N.Q. performed precision measurements of the experimentally relevant sample dimensions. The manuscript was written by P.C. and N.P.O. with input from all authors.

Additional Information:

Supplementary information is available in the online version of the paper.

Competing interests:

The authors declare no competing financial interests.

Data and materials availability:

All data will be made available and archived in Dataverse.

Supplementary Materials:

Supplementary Text

Figs. S1 to S12

References 1–9

Figure Captions:

Fig. 1. Planar thermal Hall response of α-$RuCl_3$ in the interval $0.5 < T < 10.5$ K and field range $0 < B < 13$ T with B $\parallel$ a. Panel (a) shows the B-antisymmetric thermal Hall signal $\Delta T_{\rm H}^{\rm asym}$ taken in sweep-up (red) and -down (blue) directions at 7.5 K ($\Delta T_{\rm H}^{\rm asym}$ is proportional to λ_{yx}). The inset shows the placements of thermometers measuring $T_{\rm A}$, $T_{\rm B}$ and $T_{\rm C}$. Panel (b): The color map constructed from ~ 50 traces of the thermal Hall resistivity λ_{yx} vs. B in the B-T plane (scale bar on right). The large-λ_{yx} region (in red) tapers down to a neck around 7.3 T, as $T \to 0.4$ K. Below 2.5 K, $\lambda_{yx} < 0$ in a sliver at 6.3 T (blue region). Panel (c) shows curves of λ_{yx} vs. B at fixed T. The peak in the field profiles narrows as $T \to 3.35$ K. Below 4 K, λ_{yx} is strongly suppressed to zero above 9.5 T. Panel (d) plots κ_{xy}/T vs. B (at fixed T) inferred from λ_{ij}. The non-intersecting curves imply that, at any fixed B, κ_{xy}/T is monotonic in T. Below 4.7 K the matrix inversion greatly amplifies the uncertainties in λ_{xy} for $B >9$ T. The horizontal dashed line is the half-quantized value.

Fig. 2. Curves of κ_{xy}/T vs. T at B fixed at the ten values indicated. In each panel, the solid curves are fits to Eqs. 3 and 4. At each B, the fit yields the energies ω_1 and ω_2 and $\mathcal{C}_{\rm obs}$. The grey circles represent weak deviations from the fits below 4 K. Just below the boundary of the zigzag phase ($B <7$ T), excitations in the zigzag state lead to negative deviations (see also Fig. 3b). In the QSL state ($7< B < 11$ T), positive deviations onset below 3 K and grow in amplitude as $T \to 0$. These seem to be related to the excitations that lead to oscillations in κ_{xx} (see Supplement).

Fig. 3. Bosonic edge-mode and the planar κ_{xy}. Panel(a) shows a sketch of the two lowest magnon modes (blue curves) with $\omega_1 = 11.6$ K and $\omega_2 \simeq 50$ K. With $\mathcal{C} = 1$ in the lowest band, an edge mode traverses the gap (dashed curve). The inset displays the high-intensity spots of the Berry curvature $\mathbf{\Omega}$ calculated [25] for the lowest band with $\mathbf{B} \parallel \mathbf{a}$. $\mathbf{\Omega}$ changes sign with $\mathbf{B}$. Panel (b): Curves of κ_{xy}/T vs. T with B fixed at 6.0, 6.2, 6.4 and 6.6 T (just inside the zigzag phase). Below 3 K, κ_{xy} displays a weak negative contribution. For clarity, we have shifted successive curves vertically by 0.1 mW/Km. Panel (c): The quantity $C_{\rm obs}$ defined in Eq. 6 derived from the fit at each B. As B increases, $C_{\rm obs}$ saturates to a value $\sim$1.1 above 9 T, consistent with the Chern integer 1. In the inset, the profile of $U(\mathbf{r}) + \omega_1$ is sketched as the red curve. A gradient $-\nabla T \parallel \hat{\mathbf{x}}$ unbalances the excitation densities between the warm and cool edges to produce $\mathbf{J}_{\rm Q} \parallel \hat{\mathbf{y}}$ (distribution ρ shaded in blue). Panel (d) shows

the B dependence of the energy level ω_1 derived from the fit of κ_{xy}/T vs. T to Eq. 5 at each B. At the minimum (at 6.8 T), ω_1 agrees with the energy of the narrow mode seen in ESR ($\sim$1 meV). At large B, ω_1 is slightly lower than the ESR mode, and in better agreement with the energy extracted from κ_{xx} in Ref. [11].

Extended Data Figure Captions:

Extended Data Fig. 1. Image of crystal studied in this report. The three thermometers used for temperature measurements are labeled (T_A, T_B, T_C) according to their locations.

Extended Data Fig. 2. Example of raw temperature data for a particular field-step sequence. The inset depicts the same data over a narrower time window so that the timescales for the relaxation process can be seen.

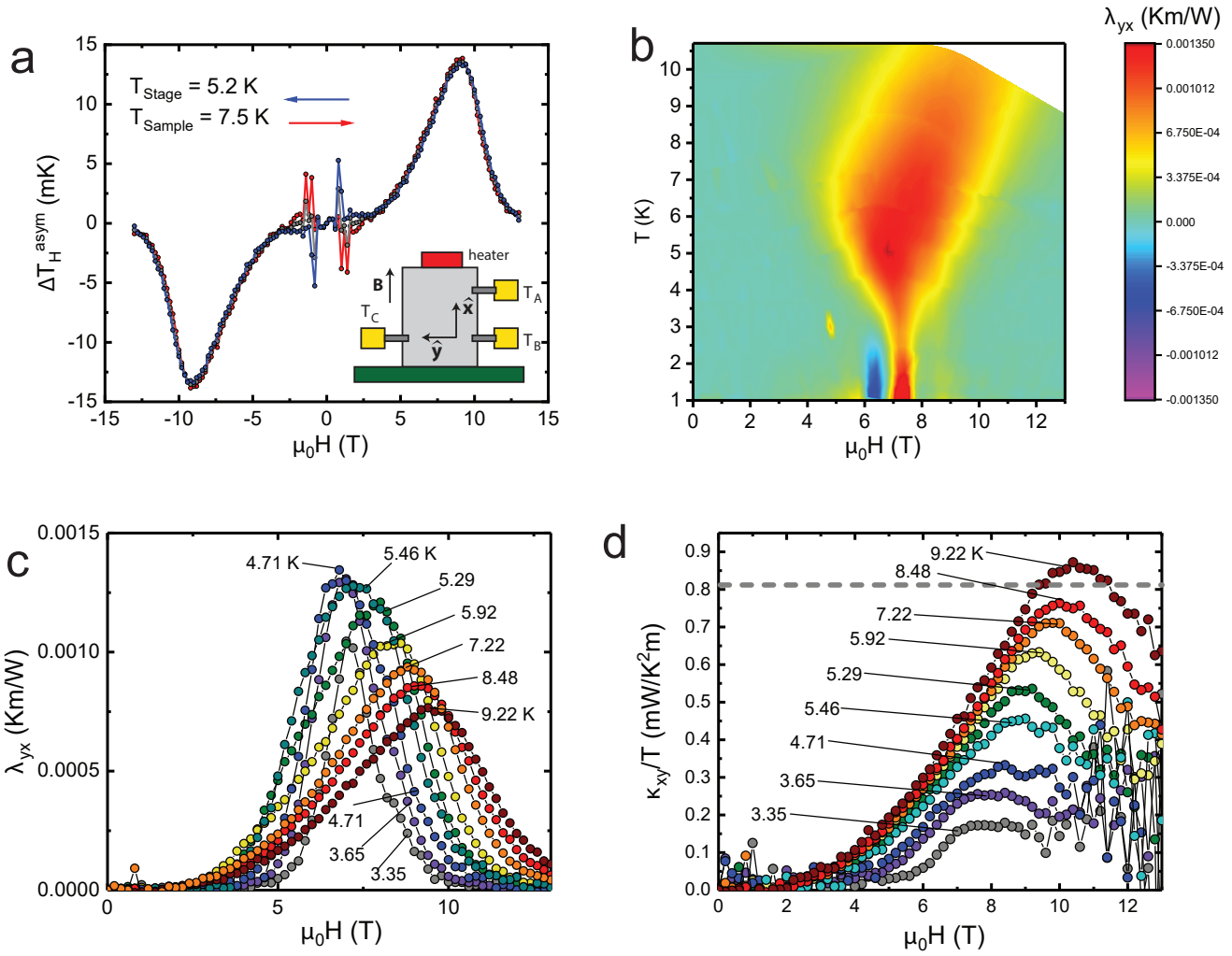
a
T_{Stage} = 5.2 K
T_{Sample} = 7.5 K
ΔT_H^{asym} (mK)
$\mu_0 H$ (T)
heater
B
T_A
T_B
T_C
$\hat{x}$
$\hat{y}$
b
λ_{yx} (Km/W)
0.001350
0.001012
6.750E-04
3.375E-04
0.000
-3.375E-04
-6.750E-04
-0.001012
-0.001350
T (K)
$\mu_0 H$ (T)
c
λ_{yx} (Km/W)
4.71 K
5.46 K
5.29
5.92
7.22
8.48
9.22 K
4.71
3.65
3.35
$\mu_0 H$ (T)
d
κ_{xy}/T (mW/K^{2}m)
9.22 K
8.48
7.22
5.92
5.29
5.46
4.71
3.65
3.35
$\mu_0 H$ (T)

FIG. 1.

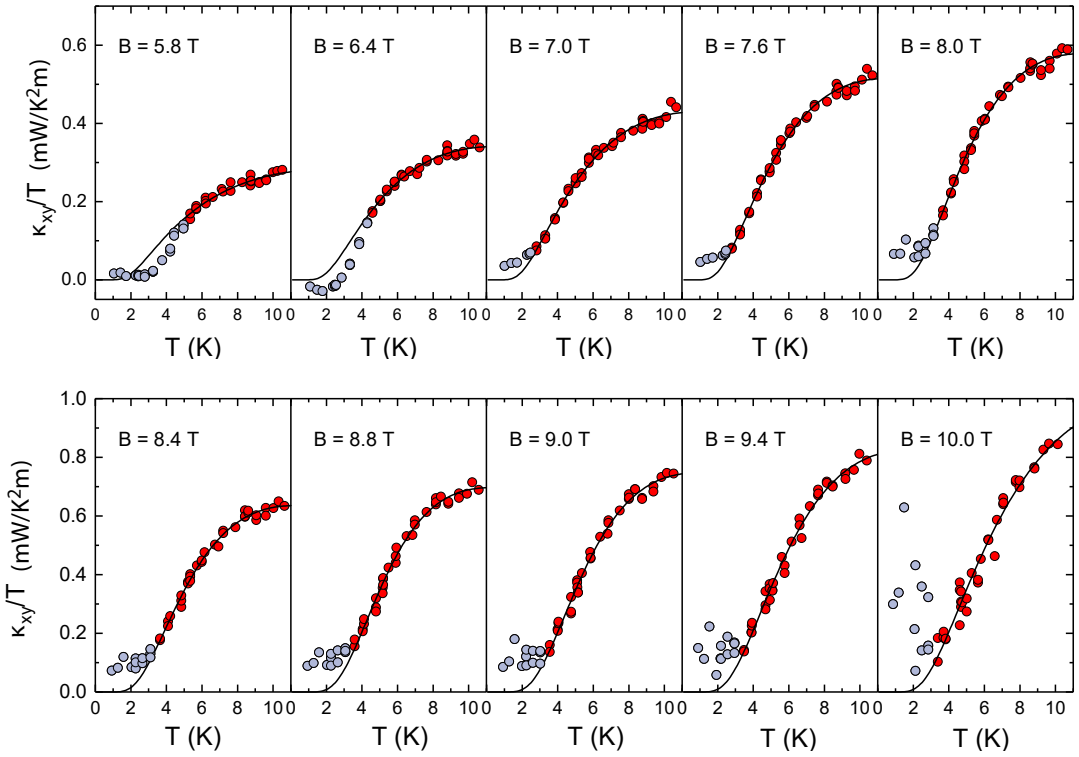
B = 5.8 T
B = 6.4 T
B = 7.0 T
B = 7.6 T
B = 8.0 T
B = 8.4 T
B = 8.8 T
B = 9.0 T
B = 9.4 T
B = 10.0 T
κxy/T (mW/K2m)
T (K)

FIG. 2.

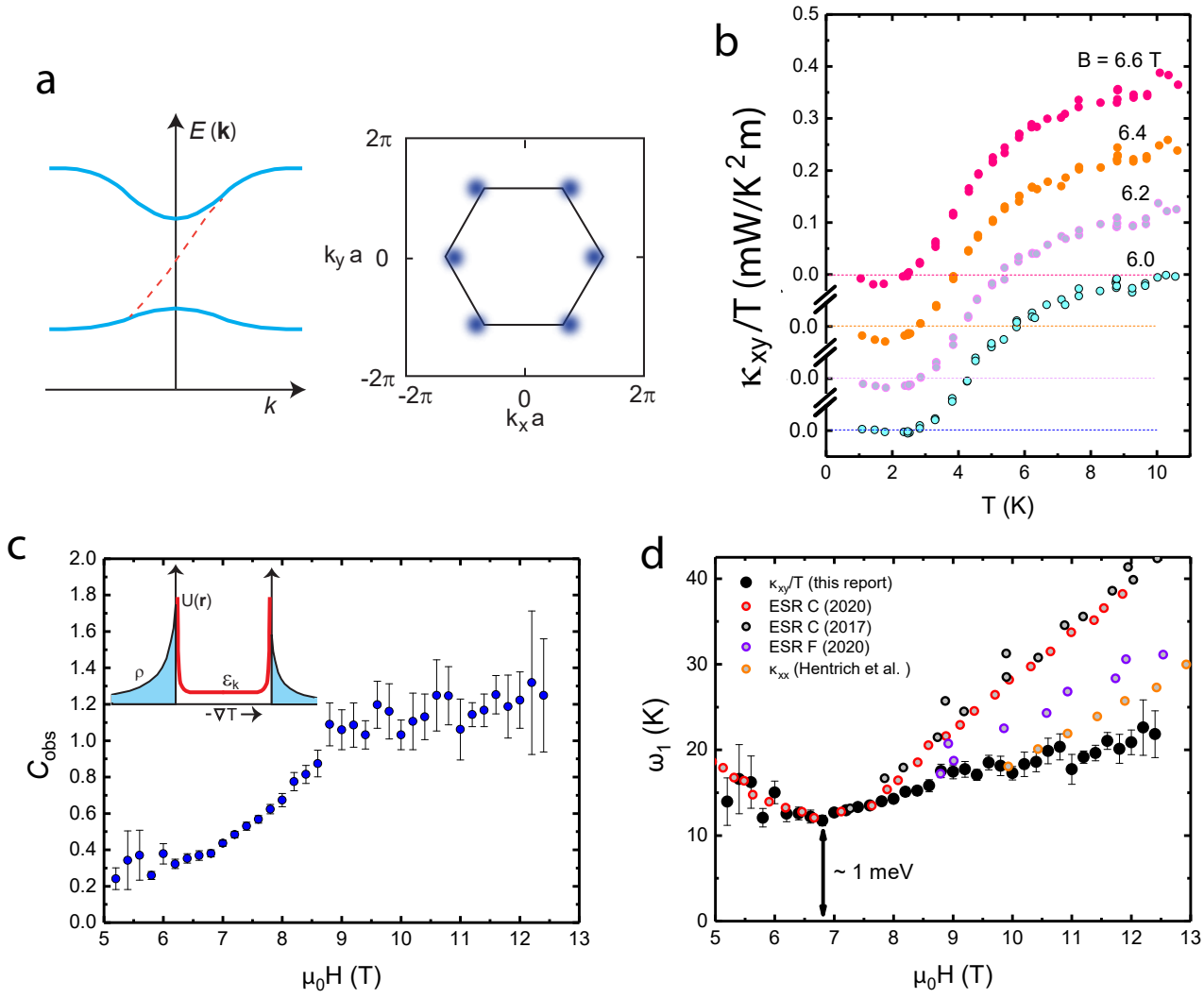
a
E (k)
k
2π
k_y a
0
-2π
-2π
0
2π
k_x a
b
B = 6.6 T
6.4
6.2
6.0
κ_xy/T (mW/K^2 m)
T (K)
c
U(r)
ρ
ε_k
-∇T
C_obs
μ_0H (T)
d
κ_xy/T (this report)
ESR C (2020)
ESR C (2017)
ESR F (2020)
κ_xx (Hentrich et al.)
~ 1 meV
ω_1 (K)
μ_0H (T)

FIG. 3.

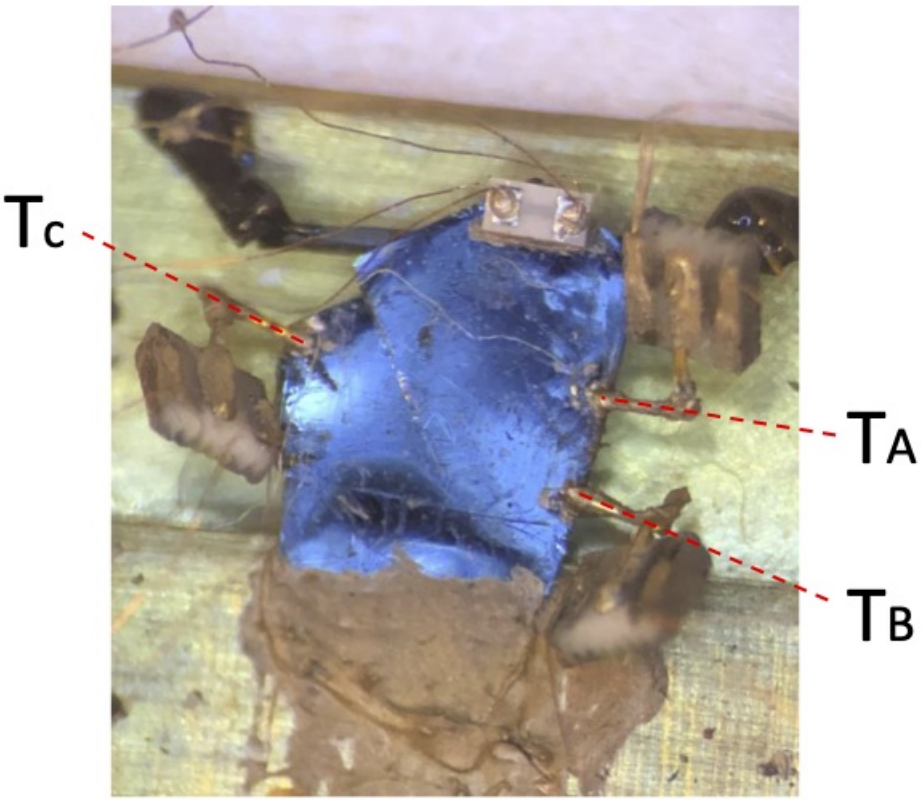

FIG. 1. **Extended Data**

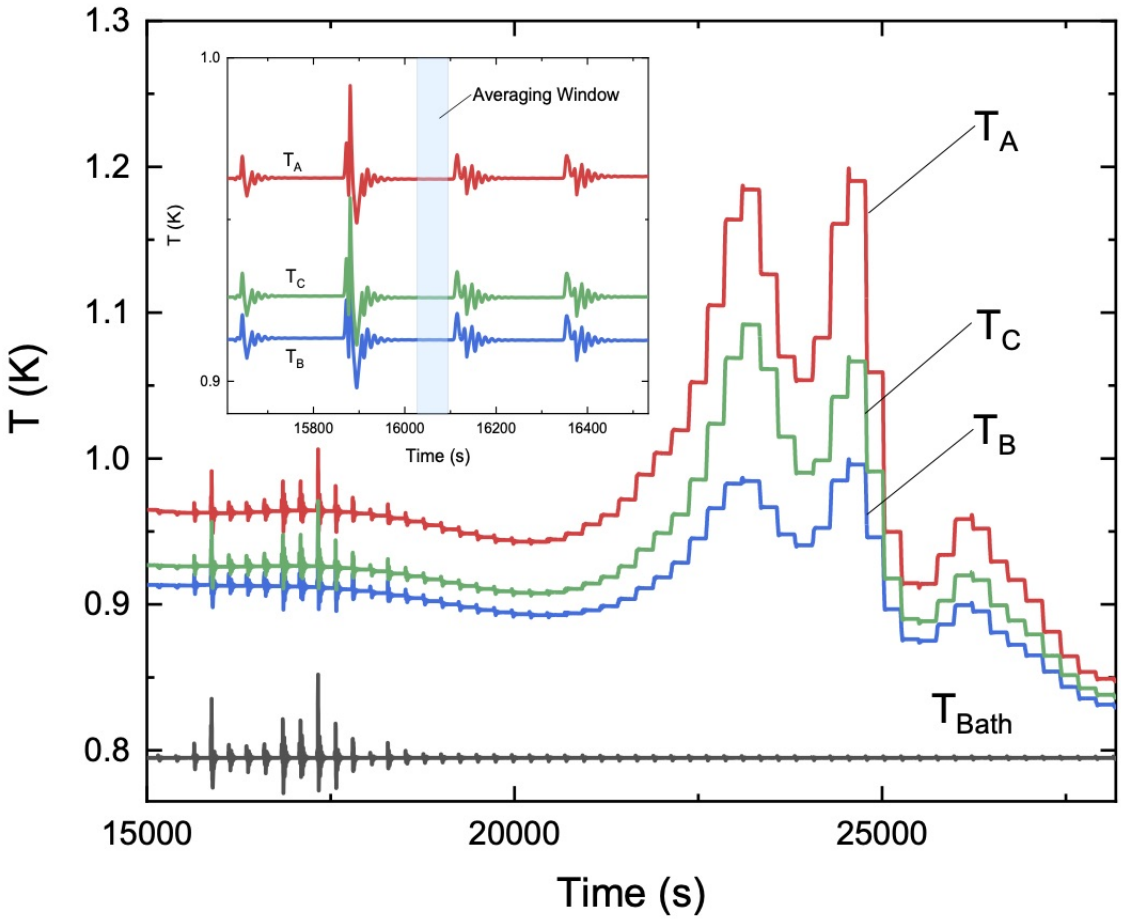

FIG. 2. **Extended Data**

Supplementary Files

This is a list of supplementary files associated with this preprint. Click to download.

- 22KxyRuCl3Supplv1.pdf